

# **Hemodynamics alteration in patient-specific dilated ascending thoracic aortas with tricuspid and bicuspid aortic valves**

Raja Jayendiran<sup>1</sup> Salvatore Campisi<sup>2</sup> Magalie Viallon<sup>3,4</sup>  
Pierre Croisille<sup>3,4</sup> and Stéphane Avril<sup>1</sup> \*

<sup>1</sup> Mines Saint-Étienne, Université de Lyon, INSERM, U1059 SaInBioSE, F-42023  
Saint-Étienne, France

<sup>2</sup> Department of Cardiovascular Surgery, University Hospital of Saint-Étienne,  
Saint-Étienne, France

<sup>3</sup> Université de Lyon, UJM-Saint-Étienne, INSA, CNRS UMR 5520, INSERM U1206,  
CREATIS, F-42023, Saint-Étienne, France

<sup>4</sup> Department of Radiology, University Hospital of Saint-Étienne, Saint-Étienne, France

Word count: 3490

---

## Abstract

In this paper, we evaluate computationally the influence of blood flow eccentricity and valve phenotype (bicuspid (BAV) and tricuspid (TAV) aortic valve) on hemodynamics in ascending thoracic aortic aneurysm (ATAA) patients. 5 TAV ATAA, 5 BAV ATAA (ascending aorta diameter  $> 35$  mm) and 2 healthy subjects underwent 4D flow MRI. The 3D velocity profiles obtained from 4D flow MRI were given as input boundary conditions to a computational fluid dynamics analysis (CFD) model. After performing the CFD analyses, we verified that the obtained time-averaged velocity profiles and flow eccentricity were in good agreement with 4D flow MRI. Then we used the CFD analyses to evaluate the time-averaged wall shear stress (TAWSS) and the local normalized helicity (LNH). We found that the flow eccentricities at the aortic root were not significantly different ( $p > 0.05$ ) between TAV and BAV phenotypes. TAWSS ( $R^2 = 0.697$ ,  $p = 0.025$ ) and absolute LNH ( $R^2 = 0.964$ ,  $p < 0.001$ ) are in good correlation with flow eccentricity. We conclude that eccentricity at the aortic root is a major determinant of hemodynamics patterns in ATAA patients regardless of the aortic valve phenotype.

*Key words:* Aneurysm, 4D flow MRI, Computational Fluid Dynamics, Biomechanics, Tricuspid and Bicuspid aortic Valve

---

\* Corresponding author. 158 cours Fauriel, 42023 Saint-Etienne cedex 2, France; Phone: +33477420188; Fax : +33477420000; Email: avril@emse.fr

# 1 Introduction

2 Ascending thoracic aortic aneurysms (ATAAs) are life-threatening pathologies characterized by pro-  
3 gressive vessel dilation. It is associated with smooth muscle cell dysfunction, occasional localized  
4 inflammatory infiltrates, and severe maladaptive extracellular matrix remodeling together predisposes  
5 the arterial wall to dissection and rupture leading to premature death (Lavall et al., 2012; Azadani  
6 et al., 2013; Real et al., 2014; Lasheras, 2007; Pasta et al., 2012). Among the etiology of ATAAs, in-  
7 dividuals with a BAV are more vulnerable to ATAA than normal TAV. Recent studies have shown that  
8 deficient TAVs also contribute to ATAA progression (Muraru et al., 2016). ATAAs progression is the  
9 result of multifactorial effects including genetics or epigenetics expressions, biomechanical (Farzaneh  
10 et al., 2018) and altered hemodynamics patterns (Girdauskas et al., 2011).

11 4D PCMRI (phase-contrast magnetic resonance imaging) also called 4D flow MRI has been com-  
12 monly used to understand aortic hemodynamics (Simao et al., 2017; Bakhshinejad et al., 2017;  
13 Biglino et al., 2015). Retrograde flows and recirculations were frequently found in BAV subjects  
14 using 4D flow MRI and it was shown that they occur at earlier age compared to TAVs (Barker et al.,  
15 2010, 2012). Moreover, hemodynamics alterations in BAV usually differ with valve fusion alterations  
16 (Bissell et al., 2013). Among hemodynamics alterations, the impact on the wall shear stress (WSS)  
17 distribution in the ascending aorta (AA) of BAV patients without concomitant valve or vessel dis-  
18 ease is significant compared with TAV subjects (Meierhofer et al., 2012). WSS responsive pathways  
19 are known to regulate endothelial function and vessel integrity (Baeyens et al., 2016). In coronary  
20 or carotid arteries, the endothelial cells exposed to high, unidirectional wall shear stress maintain a  
21 quiescent phenotype, while those exposed to low and/or directional varying WSS are activated, dis-

22 playing a pro-inflammatory phenotype (Kwak et al., 2014). Although studies related to ATAAs are  
23 scarcer, there is enough evidence to highlight essential roles of WSS in ATAA progression (Liu et al.,  
24 2014; Condemi et al., 2019; Guzzardi et al., 2015). Helicity of the flow also contributes to aneurysm  
25 progression (Youssefi et al., 2018; Pirola et al., 2018). Blood flow in the aorta possesses a significant  
26 helical component due to the complex aortic morphology (Morbiducci et al., 2013) and the helic-  
27 ity of the flow patterns can be altered in BAV patients (Garcia et al., 2017) and in ATAA patients  
28 (Frydrychowicz et al., 2012).

29 CFD is an appropriate computational method to simulate blood flows in the aorta (Yu et al., 2016;  
30 Chen et al., 2017; Bakhshinejad et al., 2017). Most of the simulation studies that have been published  
31 in the literature on this topic used idealized inlet boundary conditions rather than patient specific ve-  
32 locity maps (Pasta et al., 2013; Stevens et al., 2017). Hence there is a need to explore more accurately  
33 hemodynamics alterations related to TAVs and BAVs using CFD. The combination of 4D flow MRI  
34 and CFD presents a promising method to address this need (Callaghan et al., 2015; Romarowski et al.,  
35 2018).

36 Therefore, the main goal of this study is to characterize the effect of valve phenotype on the hemo-  
37 dynamics descriptors, namely time-averaged WSS and helicity, in the dilated ascending aortic region  
38 using CFD with inflow boundary conditions derived from 4D flow MRI. As hemodynamics calcula-  
39 tions need to be accurate, a secondary goal was to verify the accuracy of the calculations by assessing  
40 the agreement between the CFD simulations and the 4D flow MRI measurements.

## 41 **2 Methods**

### 42 *2.1 Data acquisition*

43 4D flow MRI data-sets obtained from 3T MR scanner (Magnetom Prisma, Siemens, Erlangen) were  
44 used to assess blood flows in the ascending thoracic aorta (ATA) from 12 subjects (Tab. 1). The  
45 protocol was approved by the Institutional Review Board of the University Hospital Center of Saint-  
46 Etienne and an informed consent was obtained from the participants. The axial cross sectional images  
47 at predefined anatomic levels were used for measuring the ATA maximum diameter. We measured  
48 outer to outer diameter knowing that there is no convention about measuring the luminal or outer to  
49 outer diameter of the aorta (Boehm et al., 2015). The discussion regarding the patient characteristics  
50 are given in Section B in the supplementary materials.

51 All the patients were assessed for the presence of functional valvular defects by standard transthoracic  
52 echocardiography. The echocardiographic exam relies on three parameters, namely the peak velocity,  
53 the mean pressure gradient and the aortic valve area. The first two parameters are directly calculated  
54 from Doppler, whereas the aortic valve area is derived from measurement of the left ventricular out-  
55 flow tract (LVOT) diameter, LVOT time-velocity integral (TVI) and aortic TVI using the continuity  
56 equation.

### 57 *2.2 Numerical simulation*

58 The reconstructed patient-specific geometry from 4D flow MRI data, including the ATA starting from  
59 sinotubular junction (STJ), aortic arch with branches (brachiocephalic artery (BCA), left common

60 carotid artery (LCC) & left subclavian artery (LSUB)) and the descending aorta, was imported in An-  
 61 sys Fluent (ANSYS, Academic research, Release 17.2) and meshed with tetrahedral cells for further  
 62 analysis. Details regarding the methodology are given in Section A in the supplementary materials.

### 63 2.3 Estimation of flow parameters

The flow eccentricity was calculated as follows (Condemi et al., 2019),

$$Flow_{eccentricity} = \frac{\sqrt{\sum_j (C_j - C_j^{vel})^2}}{D} \quad j = x, y, z; \quad (1)$$

64 Where  $C_j$ ,  $C_j^{vel}$  and  $D$  are the coordinates of the lumen center (Fig. S1 in the supplementary materi-  
 65 als), center of velocity and diameter, respectively.

The center of velocity  $C_j^{vel}$  was calculated as the average position of lumen pixels ( $r_i$ ), weighted by  
 the velocity information ( $v_i$ ) as given in Eq. 2 (Sigovan et al., 2011)

$$C_j^{vel} = \frac{\sum_i r_{i,j} |v_i|}{\sum_i |v_i|} \quad i = \text{lumen pixels } (x, y, z), \quad j = x, y, z; \quad (2)$$

66 Flow eccentricity equal to 0 indicates that the flow is centrally distributed along the length of the  
 67 vessel and 1 indicates that the flow is fully eccentric.

The local normalized helicity (LNH) corresponds to the local value of the cosine of the angle between  
 the velocity  $V$  and vorticity  $\omega$  (Garcia et al., 2017)

$$LNH = \frac{V \cdot \omega}{|V| |\omega|} \quad (3)$$

68 LNH varies between -1 (left-handed rotation) and 1 (right-handed rotation) with 0 indicating a sym-  
69 metrical flow (Manuel et al., 2009; Condemi et al., 2017). [An optimal LNH threshold detecting dif-](#)  
70 [ferences between patients and the healthy group is set as 0.6 based on the study conducted by Garcia](#)  
71 [et al. \(2017\)](#). At each threshold the percentage of the total volume occupied by the isosurface volume  
72 was assessed.. For example, the % volume of absolute  $LNH \geq 0.6$  was calculated from the iso-surface  
73 volume ( $\% \text{ volume of absolute } LNH \geq 0.6 = \text{volume of absolute } LNH \geq 0.6 / \text{Total volume} \times 100$ ).

The TAWSS value was calculated such as (Condemi et al., 2019),

$$TAWSS = \frac{1}{T} \int_0^T WSS \, dt \quad (4)$$

74 where T is the period of the cardiac cycle and WSS is the instantaneous wall shear stress. The %  
75 surface area with  $TAWSS \leq 1 \text{ Pa}$  was derived, being defined as the surface area with  $TAWSS \leq 1 \text{ Pa}$   
76 /Total surface area  $\times 100$ .

#### 77 2.4 Statistical analyses

78 The statistical analysis was performed with SPSS 17 (IBM SPSS software, Chicago). A Bland Altman  
79 analysis was performed to evaluate the agreement between the CFD simulation and the 4D flow  
80 MRI measured flow eccentricity. A 2-tailed independent samples t-test was conducted to evaluate  
81 the significant differences between TAV and BAV ATAAs. The deduced parameters namely flow  
82 eccentricity, TAWSS and absolute LNH in the ATA between TAV and BAV were compared using an  
83 independent-sample t-test. A pre-determined level of significance equal to 95% and p-values  $< 0.05$   
84 were considered as significant.

## 85 **3 Results**

### 86 *3.1 Comparison between CFD-calculated vs. 4D flow MRI- measured velocities and flows*

87 In order to ensure that the velocity profiles obtained from 4D flow MRI at different time frames  
88 throughout the cardiac cycle are correctly estimated by CFD, we have compared the time-averaged  
89 velocity profiles from CFD simulations with the 4D flow MRI. Agreement between the 4D flow MRI  
90 and CFD profiles should be satisfied as the former was used to assign boundary conditions of the  
91 latter. However, interpolation was required to assign the boundary conditions at the correct times as  
92 time steps of the CFD analysis did not coincide with the times at which the MRI data were acquired.  
93 The time-averaged velocity profiles obtained from 4D flow MRI and CFD are shown in Fig. 1.

94 Flow eccentricity calculated near the dilated region (section 2-2' i.e largest diameter in the dilated  
95 region shown in Fig. S2) from 4D flow MRI during the systolic phase was compared with the CFD  
96 simulations using Bland-Altman plot. The estimated bias was -0.01085, standard deviation of bias  
97 was 0.0353, the 95% limits of agreement varied from -0.080 (blue dotted line) to 0.058 (red dashed  
98 line) and the continuous brown line represents the mean (Fig. 2). All data points remained in the  
99 95% limit band (average difference  $\pm 1.96$  standard deviation of the difference), indicating the good  
100 agreement between the 4D flow MRI measurements and the CFD simulation quantitatively.

### 101 *3.2 Streamlines*

102 The streamlines obtained from the simulations at peak systole for different cases are shown in Fig 3.  
103 The streamline contours for both BAV and TAV ATAA patients showed that the flow starts detaching

104 from the aortic wall and a vortex is formed near the dilated ATA region. In healthy subjects the flow is  
105 found to be laminar and evenly distributed through the cross-section of the aorta near the ATA region.

### 106 3.3 TAWSS

107 TAWSS was obtained for TAV ATAA, BAV ATAA and healthy subjects (Figs. 4, 5, & 6). Both TAV  
108 ATAA and BAV ATAA patients exhibited low TAWSS (i.e  $\leq 1$  Pa) in the ATA region. The surface  
109 area of the ATA with TAWSS  $\geq 3$  Pa and  $\leq 1$  Pa were evaluated (Tab. 2). Irrespectively of the valve  
110 phenotype, all patients, except patient 4, have large surface area (i.e varying between 70% and 99%)  
111 with low TAWSS (i.e  $\leq 1$  Pa). High TAWSS (i.e  $\geq 3$  Pa) were found only in small regions ( $\leq 1\%$   
112 surface area) of the ATA in 8 out of 10 patients, whereas patient 6 and 8 have 8% and 7% of the  
113 surface area with TAWSS  $\geq 3$  Pa. Healthy subjects have surface area  $\geq 25\%$  with high TAWSS ( $\geq 3$   
114 Pa) and  $\approx 20\%$  surface area with low TAWSS ( $\leq 1\%$ ).

### 115 3.4 Helicity

116 The LNH magnitude was extracted for all patients and healthy subjects (Figs. 4, 5, & 6). It was ob-  
117 served that large absolute LNH values were more prominent in ATAA patients than healthy subjects.  
118 In ATAA patients the % volume with absolute LNH  $\geq 0.6$  is  $> 2$  and absolute LNH  $\leq 0.4$  varies  
119 between 80 and 95. In healthy subjects, more than 98% volume has an absolute LNH below 0.4 and  
120 less than 1% volume has absolute LNH  $\geq 0.6$  (Tab. 2).

### 121 3.5 Correlation between flow eccentricity and hemodynamics descriptors

122 A significant correlation is obtained between flow eccentricity at section 2-2' = ascending aortic  
123 region with maximum diameter and flow eccentricity at section 1-1' = sinotubular junction - also  
124 referred as aortic inlet in this paper. Hence, we also studied correlation between flow eccentricity at  
125 section 2-2' and WSS, TAWSS and LNH biomarkers. Figure 7 summarizes the independent associa-  
126 tions between parameters such as flow eccentricity at section 1-1', % surface area with TAWSS  $\leq$  1  
127 Pa, % volume with absolute LNH  $\geq$  0.6, maximal ATAA diameter and inlet angle with flow eccen-  
128 tricity at section 2-2'. Strong and significant correlations exist between flow eccentricity at section  
129 1-1' ( $R^2 = 0.655$ ,  $p = 0.040$ ), % surface area with TAWSS  $\leq$  1 Pa ( $R^2 = 0.697$ ,  $p = 0.025$ ), % volume  
130 with absolute LNH  $\geq$  0.6 ( $R^2 = 0.964$ ,  $P < 0.001$ ), maximal ATAA diameter ( $R^2 = 0.664$ ,  $p = 0.036$ )  
131 with flow eccentricity at section 2-2'. But there is no significant relationship between the inlet angle  
132 ( $R^2 = 0.261$ ,  $p = 0.467$ ) and the flow eccentricity at section 2-2'.

### 133 3.6 Correlation between maximum ATAA diameter and hemodynamics descriptors

134 A significant correlation was found between the diameter and hemodynamics descriptors namely  
135 TAWSS and helicity (Fig. 8). For instance, regarding the % of surface area with TAWSS  $\leq$  1 Pa  
136 significance is valued at  $R^2 = 0.688$ ,  $p = 0.028$  and for the % of volume with absolute LNH  $\geq$  0.6  
137 significance is valued at  $R^2 = 0.650$ ,  $p = 0.045$ . The increase in maximal ATAA diameter affects the  
138 hemodynamics descriptors for both TAV ATAA and BAV ATAA patients.

### 139 3.7 Significance of differences in hemodynamics descriptors between TAV and BAV ATAA patients

140 Hemodynamics descriptors, namely flow eccentricity, TAWSS and helicity in TAV and BAV groups  
141 were compared using 2-tailed independent samples t-test . Results are reported in Tab. 1. The data  
142 are presented as mean  $\pm$  standard deviation (max,min). The parameters such as flow eccentricity at  
143 section 1-1' (p = 0.268), flow eccentricity at section 2-2' (p = 0.575), % surface area with TAWSS  
144  $\geq 3$  Pa (p = 0.282), % surface area with TAWSS  $\leq 1$  Pa (p = 0.483), % volume with absolute LNH  
145  $\geq 0.6$  (p = 0.367) and % volume with absolute LNH  $\leq 0.4$  (p = 0.235) have a p-value  $> 0.05$ . The  
146 significance  $> 0.05$  shows that the hemodynamics descriptors obtained from TAV and BAV patient  
147 were not significantly different.

## 148 4 Discussion

149 This study showed that flow eccentricity at the aortic root is a major determinant of hemodynamics  
150 alterations in ATAAs, such as low TAWSS and elevated absolute LNH values are independent of the  
151 aortic valve phenotype. The flow eccentricity at the aortic root indicates a dysfunction of the aortic  
152 valve and is frequent with BAV phenotype. But the relation between eccentricity downstream and  
153 WSS, TAWSS & LNH biomarkers remains to be elucidated, especially how the enlargement of aortic  
154 diameter in aneurysms participates to increase the flow disturbance caused by eccentricity at the aortic  
155 root.

156 Our CFD simulations are time resolved and provide estimations of the velocity maps at different  
157 timeframes. Only after running the simulations, at the post-processing stage, we eventually compute

158 time averaged metrics to compare the groups of subjects. The time-averaged velocities obtained from  
159 CFD analyses were validated against MRI data justifying the significance of time-averaged metrics  
160 derived from CFD analyses.

161 Among studies related to BAV and TAV patients, Hope et al. (2011) and Pasta et al. (2013) compared  
162 the blood flow patterns between TAV and BAV in patients harbouring ATAA. One of the two was  
163 based on 4D flow MRI to measure *in vivo* 3D blood flow velocities in the aorta, finding abnormal  
164 eccentric flow and asymmetric WSS for both BAV and TAV patients (Hope et al., 2011). The other  
165 study was based on CFD simulations, showing a slight difference in the helical flow patterns between  
166 TAV and BAV ATAA patients (Pasta et al., 2013) but they did not consider patient specific velocity  
167 patterns. Our study proposed a framework combining 4D flow MRI and CFD to compute ATAA  
168 hemodynamics.

169 We found that blood flow disturbance near the dilated region generates vortices in TAV and BAV  
170 ATAAs and not in the healthy subjects (Weigang et al., 2008; Sigovan et al., 2011; Pasta et al., 2013;  
171 Numata et al., 2016). The flow disturbance refers here to the existence of retrograde flows and recir-  
172 culation areas (Chiu and Chien, 2011). The vortices manifest with flow eccentricity and non-uniform  
173 distribution of WSS, potentially causing accumulation of atherogenic particles at the endothelial sur-  
174 face (Deng et al., 2008; Ethier, 2002; Tarbell, 2003; Chiu and Chien, 2011).

175 As we assumed rigid and impermeable walls (Torii et al., 2009; Steinman, 2012), we focused our  
176 analysis on TAWSS values only, not on temporal variations of WSS. TAWSS contours of both TAV  
177 and BAV ATAAs show large areas with TAWSS lower than 1 Pa. In healthy subjects the area fraction  
178 occupied by  $TAWSS \leq 1$  Pa and  $\geq 3$  Pa was significantly lower. The increase in flow eccentricity

179 near the dilated region induces a decrease of the TAWSS magnitude. More surface is occupied by  
180 low TAWSS in TAV and BAV ATAAs. Commonly TAWSS in healthy arteries is between 1 and 7  
181 Pa (Nordgaard et al., 2010). Low TAWSS (i.e.  $\leq 1$  Pa) in a large area fraction of the aortic vessel  
182 indicates possible endothelial dysfunction and progress in vascular disease (Nordgaard et al., 2010;  
183 Papadopoulos et al., 2016; Numata et al., 2016). If the TAWSS is larger than 7 Pa, endothelial damage  
184 can also be induced but the mechanisms of this damage have not yet been fully elucidated (Fukumoto  
185 et al., 2008). TAWSS also shows good correlation with maximal ATAA diameter. With increased  
186 ATAA diameter, the percentage of area with low TAWSS increases.

187 LNH contours show that both TAV ATAA and BAV ATAA have large volumes with elevated absolute  
188 LNH (i.e.  $\geq 0.6$ ) compared to healthy subjects. These results are in agreement with previous studies  
189 where elevated helicity was found in ATAA patients (Lorenz et al., 2014; Garcia et al., 2017). It was  
190 observed that the % volume of absolute LNH  $\geq 0.6$  had a significant correlation with flow eccentricity  
191 and maximal ATAA diameter. Eventhough there are many studies indicating the role of helicity in the  
192 development of cardiovascular diseases (Kilner et al., 1993; Caro et al., 1996; Stonebridge et al., 1996;  
193 Morbiducci et al., 2007; Liu et al., 2009, 2014), it is yet unclear how these hemodynamics alterations  
194 affect wall remodeling in ATAAs (Gataulin et al., 2015; Ha et al., 2016).

195 The correlation analysis between the aortic valve phenotype and the hemodynamics descriptors shows  
196 that TAV and BAV ATAA patients have no significant difference in terms of blood flow patterns and  
197 hemodynamics descriptors (refer Tab. 1). Patients with both aortic valve phenotypes have shown more  
198 region with low TAWSS, elevated absolute LNH and pronounced flow eccentricity near the dilated  
199 ATA region. Irrespective of the aortic valve phenotype the alteration in hemodynamics parameters  
200 was due to flow eccentricity patterns.

201 Basically the aortic valve condition should be classified based on:

202 1) the morphological condition (phenotype) which relates to the natural feature of the valve (BAV or  
203 TAV)

204 2) the functional condition which relates to the behaviour of the valve during the cardiac cycle. It can  
205 be quantified in terms of hemodynamics descriptor, namely the flow eccentricity

206 In the present work we have shown that both BAV and TAV can have similar functional conditions.  
207 This may explain why it is very difficult to establish correlations between the valve phenotype and  
208 the aneurysm rupture risk (Agnese et al., 2019; Forsell et al., 2014; Kjellqvist et al., 2013; Ikonomidis  
209 et al., 2007; Corte et al., 2008).

210 In our 5 BAV patients, only two of them presented a mild degree of AR, the rest had BAV phenotypes  
211 without any gradient or AR degree. Accordingly, the functional status of the aortic valve seems to in-  
212 fluence the ATA flow patterns. This was also previously demonstrated for AS, with good correlations  
213 between the AS degree and ATAA flow patterns (Farag et al., 2018). Moreover, almost 50% of BAV  
214 patients never develop ATAA and keep normal functions during the entire lifetime without treatment  
215 (Pedersen et al., 2019). Reciprocally, diseased tri-leaflet aortic valves can acquire abnormal opening  
216 just like bi-leaflet valves inducing eccentric flows at the aortic root. Therefore, the aortic valve func-  
217 tional condition (characterized by flow eccentricity at the aortic root) rather than the phenotype is a  
218 major factor in determining hemodynamics alterations in the ATA (Fig. 3).

219 There are some limitations in this study. The sample size was limited to 10 patients and 2 healthy  
220 subjects. [Ooij et al. \(2017\)](#) found significant differences in peak systolic WSS between a large group  
221 of BAV (n = 136) and TAV (n = 213) with no AS. In the present study we could not find any differences

222 between TAWSS in BAV and TAV. It may be due to the small sample size and/or the fact that averaging  
223 out WSS patterns over time is not accurate enough to detect differences.

224 CFD simulations were based on the assumption of rigid and impermeable walls. The comparison  
225 between the CFD and 4D flow MRI time-averaged velocity maps shows some differences in some pa-  
226 tients. This may be induced by the interpolation effects, but also due to outlet boundary conditions and  
227 the rigid wall assumption. These assumptions are usually reasonable for flow and WSS predictions  
228 in finite segments of large arteries (Steinman, 2012) although they may induce errors in evaluating  
229 temporal variations of WSS. The velocity distribution obtained from 4D flow MRI was used as inlet  
230 boundary condition for the simulation. As 4D flow MRI datasets are noisy, this can be transmitted  
231 to the computational predictions. However these datasets permit to assign patient-specific boundary  
232 conditions to the model, which is essential for modelling hemodynamics computationally.

## 233 **5 Conclusions**

234 This study demonstrated that the flow eccentricity at the aortic root influences the blood flow patterns  
235 in ATAA patients independently of the aortic valve phenotype. Flow eccentricity values across the  
236 dilated region have significant correlation with TAWSS, absolute LNH and maximal ATAA diameter,  
237 however they have no correlation with the inlet angle. Knowing the critical role of flow eccentricity in  
238 hemodynamics alterations, it will be important to determine how it interacts with other critical factors  
239 of ATAA such as aortic wall remodeling and smooth muscle cell differentiation.

## 240 **Acknowledgments**

241 This research work was supported by the European Research Council (ERC grant biolochanics, grant  
242 number 647067). We are also grateful to Ansys, Inc. for providing Ansys Fluent (ANSYS<sup>®</sup> Aca-  
243 demic Research, Release 17.2).

## 244 **6 Conflict of interest**

245 There is no conflict of interest.

## 246 **References**

- 247 Agnese, V., Pasta, S., Michelena, H.I., Mina, C., Romano, G.M., Carerj, S., Zito, C., Maalouf, J.F.,  
248 Foley, T.A., Raffa, G., Clemenza, F., Pilato, M., Bellavia, D., 2019. Patterns of ascending aortic di-  
249 latation and predictors of surgical replacement of the aorta: A comparison of bicuspid and tricuspid  
250 aortic valve patients over eight years of follow-up. *J. Mol. Cell. Cardiol.* 135, 31 – 39.
- 251 Azadani, A.N., Chitsaz, S., Mannion, A., Mookhoek, A., Wisneski, A., Guccione, J.M., Hope, M.D.,  
252 Ge, L., Tseng, E.E., 2013. Biomechanical Properties of Human Ascending Thoracic Aortic  
253 Aneurysms. *Ann. Thorac. Surg.* 9, 50–58.
- 254 Baeyens, N., Bandyopadhyay, C., Coon, B.G., Yun, S., Schwartz, M.A., 2016. Endothelial fluid shear  
255 stress sensing in vascular health and disease. *J. Clin. Invest.* 126, 821–828.
- 256 Bakhshinejad, A., Baghaie, A., Vali, A., Saloner, D., Rayz, V.L., D’Souza, R.M., 2017. Merging

257 computational fluid dynamics and 4d flow mri using proper orthogonal decomposition and ridge  
258 regression. *J. Biomech.* 58, 162–173.

259 Barker, A.J., Lanning, C., Shandas, R., 2010. Quantification of hemodynamic wall shear stress in  
260 patients with bicuspid aortic valve using phase-contrast MRI. *Ann. Biomed. Eng.* 38, 788 – 800.

261 Barker, A.J., Markl, M., Burk, J., Lorenz, R., Bock, J., Bauer, S., Schulz-Menger, J., Brenkenhoff,  
262 F.V.K., 2012. Bicuspid Aortic Valve Is Associated With Altered Wall Shear Stress in the Ascending  
263 Aorta. *Circ. Cardiovasc. Imag.* 5, 457 – 466.

264 Biglino, G., Cosentino, D., Steeden, J.A., Nova, L.D., Castelli, M., Ntsinjana, H., Pennati, G., Taylor,  
265 A.M., Schievano, S., 2015. Using 4D Cardiovascular Magnetic Resonance Imaging to Validate  
266 Computational Fluid Dynamics: A Case Study. *Front. Pediatr.* 3, 1–10.

267 Bissell, M.M., Hess, A.T., Biasioli, L., Glaze, S.J., Loudon, M., Pitcher, A., Davis, A., Prendergast,  
268 B., Markl, M., Barker, A.J., Neubauer, S., Myerson, S.G., 2013. Aortic Dilation in Bicuspid Aortic  
269 Valve Disease. *Circ. Cardiovasc. Imag.* 86, 499–507.

270 Boehm, N.K., Maceira, A., Buechel, E.R.V., Claussen, J.V., Turkbey, E.B., Williams, R., Plain, S.,  
271 Tee, M., Eng, J., Bluemke, D.A., 2015. Normal values for cardiovascular magnetic resonance in  
272 adults and children. *J. Cardiovasc. Magn. Reson.* , 17–29.

273 Callaghan, F.M., Karkouri, J., Broadhouse, K., Evin, M., Fletcher, D.F., Grieve, S.M., 2015. Tho-  
274 racic aortic aneurysm: 4D flow MRI and computational fluid dynamics model. *Comput. Methods*  
275 *Biomech. Biomed. Eng.* 18, 1894–1895.

276 Caro, C.G., Doorly, D.J., Tarnawski, M., Scott, K.T., Long, Q., Dumoulin, C.L., 1996. Non-planar  
277 curvature and branching of arteries and non-planar-type flow. *Proc. Roy. Soc. A* 452, 185–197.

278 Chen, Z., Yu, H., Shi, Y., Zhu, M., Wang, Y., Hu, X., Zhang, Y., Chang, Y., Xu, M., Gao, W., 2017.  
279 Vascular Remodelling Relates to an Elevated Oscillatory Shear Index and Relative Residence Time

280 in Spontaneously Hypertensive rats. *Scientific Reports* 7, 1–10.

281 Chiu, J.J., Chien, S., 2011. Effects of Disturbed Flow on Vascular Endothelium: Pathophysiological  
282 Basis and Clinical Perspectives. *Phys. Rev.* 91, 327–387.

283 Condemi, F., Campisi, S., Viallon, M., Croisille, P., Avril, S., 2019. Relationship between ascending  
284 thoracic aortic aneurysms hemodynamics and biomechanical properties. *IEEE Trans. Biomed. Eng.*  
285 <https://doi.org/10.1109/TMI.2019.2924955>.

286 Condemi, F., Campisi, S., Viallon, M., Troalen, T., Xuexin, G., Barker, A.J., Markl, M., Croisille,  
287 P., Trabelsi, O., Cavinato, C., Duprey, A., Avril, S., 2017. Fluid- and Biomechanical Analysis of  
288 Ascending Thoracic Aorta Aneurysm with Concomitant Aortic Insufficiency. *Ann. Biomed. Eng.*  
289 45, 2921–2932.

290 Corte, A.D., Quarto, C., Bancone, C., Castaldo, C., Meglio, F.D., Nurzynska, D., Santo, L.S.D., Feo,  
291 M.D., Scardone, M., Montagnani, S., Cotrufo, M., 2008. Spatiotemporal patterns of smooth muscle  
292 cell changes in ascending aortic dilatation with bicuspid and tricuspid aortic valve stenosis: Focus  
293 on cell-matrix signaling. *J. Thorac. Cardiovasc. Surg.* 135, 8 – 18.

294 Deng, X., Marois, Y., How, T., Merhi, Y., King, M., Guidoin, R., Karino, T., 2008. Luminal surface  
295 concentration of lipoprotein (LDL) and its effect on the wall uptake of cholesterol by canine carotid  
296 arteries. *J. Vasc. Surg.* 21, 135–145.

297 Ethier, C.R., 2002. Computational modeling of mass transfer and links to atherosclerosis. *Ann.*  
298 *Biomed. Eng.* 30, 461–471.

299 Farag, E.S., Ooij, P.V., Planken, R.N., Dukker, K.C.P., d. Heer, F., Bouma, B.J., Visser, D.R.,  
300 Groenink, M., Nederveen, A.J., d. Mol, B.A.J.M., Kluin, J., Boekholdt, S.M., 2018. Aortic valve  
301 stenosis and aortic diameters determine the extent of increased wall shear stress in bicuspid aortic  
302 valve disease. *J. Mag. Res. Imag.* 48, 522 – 530.

303 Farzaneh, S., Trabelsi, O., Avril, S., 2018. Inverse identification of local stiffness across ascending  
304 thoracic aortic aneurysms. *Biomechan. Model. Mechanobiol.* [https://doi.org/10.1007/s10237-018-](https://doi.org/10.1007/s10237-018-1073-0)  
305 1073-0.

306 Forsell, C., Bjorck, H.M., Eriksson, P., Cereceda, A.F., Gasser, T.C., 2014. Biomechanical Proper-  
307 ties of the Thoracic Aneurysmal Wall: Differences Between Bicuspid Aortic Valve and Tricuspid  
308 Aortic Valve Patients. *Ann. Thorac. Surg.* 98, 65 – 71.

309 Frydrychowicz, A., Berger, A., Rio, A.M.D., Russe, M.F., Bock, J., Harloff, A., Markl, M., 2012.  
310 Interdependencies of aortic arch secondary flow patterns, geometry, and age analysed by 4-  
311 dimensional phase contrast magnetic resonance imaging at 3 tesla. *Euro. Radiol.* 22, 1122–1130.

312 Fukumoto, Y., Hiro, T., Fujii, T., Hashimoto, G., Fujimura, T., Yamada, J., Okamura, T., Matsuzaki,  
313 M., 2008. Localized Elevation of Shear Stress Is Related to Coronary Plaque Rupture: A 3-  
314 Dimensional Intravascular Ultrasound Study With In-Vivo Color Mapping of Shear Stress Dis-  
315 tribution. *J. Amer. Collg. Cardio.* 51, 645–650.

316 Garcia, J., Barker, A.J., Collins, J.D., Carr, J.C., Markl, M., 2017. Volumetric quantification of ab-  
317 solute local normalized helicity in patients with bicuspid aortic valve and aortic dilatation. *Magn.*  
318 *Reson. Med.* 78, 689–701.

319 Gataulin, Y.A., Zaitsev, D.K., Smirnov, E.M., Fedorova, E.A., Yukhnev, A.D., 2015. Weakly swirling  
320 flow in a model of blood vessel with stenosis: Numerical and experimental study. *St. Petersburg*  
321 *Polytechnical University Journal: Physics and Mathematics* 1, 364–371.

322 Girdauskas, E., Borger, M.A., Secknus, M.A., Girdauskas, G., Kuntze, T., 2011. Is aortopathy in  
323 bicuspid aortic valve disease a congenital defect or a result of abnormal hemodynamics? A critical  
324 reappraisal of a one-sided argument. *Euro. J. Cardio. Thora.surg* 39, 809 – 814.

325 Guzzardi, D.G., Baker, A.J., Ooij, P.V., Malaisrie, S.C., Putjumana, J.J., Belke, D.D., Mewhort,

326 H.E.M., Svystonyuk, D.A., Kang, S., Verma, S., Collins, J., Carr, J., Bonow, R.O., Markl, M.,  
327 Thomas, J.D., McCarthy, P.M., Fedak, P.W.M., 2015. Valve-Related Hemodynamics Mediate Hu-  
328 man Bicuspid Aortopathy. *J. Amer. Collg. Cardio.* 66, 892 – 900.

329 Ha, H., Kim, G.B., Kweon, J., Lee, S.J., Kim, Y.H., Kim, N., Yang, D.H., 2016. The influence of the  
330 aortic valve angle on the hemodynamic features of the thoracic aorta. *Scientific Reports* 6, 1–14.

331 Hope, M.D., Hope, T.A., Crook, S.E., Ordovas, K.G., Urbania, T.H., Alley, M.T., Higgins, C.B.,  
332 2011. 4D flow CMR in assessment of valve-related ascending aortic disease. *J. Amer. Collg.*  
333 *Cardio.: Cardiovascular Imaging* 4, 781 – 7.

334 Ikonomidis, J.S., Jones, J.A., Barbour, J.R., Stroud, R.E., Clark, L.L., Kaplan, B.S., Zeeshan, A.,  
335 Bavaria, J.E., Gorman, J.H., Spinale, F.G., Gorman, R.C., 2007. Expression of matrix metallopro-  
336 teinases and endogenousinhibitors within ascending aortic aneurysms of patientswith bicuspid or  
337 tricuspid aortic valves. *J. Thorac. Cardiovasc. Surg.* 133, 1028 – 1036.

338 Jayendiran, R., Condemi, F., Campisi, S., Viallon, M., Croisille, P., Avril, S., 2020. Compu-  
339 tational prediction of hemodynamical and biomechanical alterations induced by aneurysm di-  
340 latation in patient-specific ascending thoracic aortas. *Int. J. Numer. Methods.Biomed. Eng.*  
341 <https://doi.org/10.1002/cnm.3326>.

342 Kilner, P.J., Yang, G.Z., Mohiaddin, R.H., Firmin, D.N., Longmore, D.B., 1993. Helical and retro-  
343 grade secondary flow patterns in the aortic arch studied by three -directional magnetic resonance  
344 velocity mapping. *Circulation* 88, 2235–2247.

345 Kjellqvist, S., Maleki, S., Olsson, T., Chwastyniak, M., Branca, R.M.M., Lehtio, J., Pinet, F., cere-  
346 ceda, A.F., Eriksson, P., 2013. A combined proteomic and transcriptomic approach shows diverging  
347 molecular mechanisms in thoracic aortic aneurysm development in patients with tricuspidand bi-  
348 cuspid aortic valve. *Mol. Cell. Prot.* 12, 407 – 425.

349 Kwak, B.R., Back, M., Piallat, M.L.B., Caligiuri, G., Daemen, M.J.A.P., Davies, P.F., Hofer, I.E.,  
350 Holvoet, P., Jo, H., Krams, R., Lehoux, S., Monaco, C., Steffens, S., Virmani, R., Weber, C.,  
351 Wentzel, J.J., Evans, P.C., 2014. Biomechanical factors in atherosclerosis: mechanisms and clinical  
352 implications. *Euro. Heart J.* 35, 3013–3020.

353 Lasheras, J.C., 2007. The Biomechanics of Arterial Aneurysms. *Annu. Rev. Fluid Mech.* 39, 293–  
354 319.

355 Lavall, D., Schafers, H.J., Bohm, M., Laufs, U., 2012. Aneurysms of the ascending aorta. *Deutsches*  
356 *Arzteblatt International* 109, 227–233.

357 Liu, X., Pu, F., Fan, Y., Deng, X., Li, D., Li, S., 2009. A numerical study on the flow of blood and  
358 the transport of LDL in the human aorta : the physiological significance of the helical flow in the  
359 aortic arch. *Amer. J. Phy. Heart. Cir. Phy.* 297, H163–H170.

360 Liu, X., Sun, A., Fan, Y., Deng, X., 2014. Physiological Significance of Helical Flow in the Arterial  
361 System and its Potential Clinical Applications. *Ann. Biomed. Eng.* 43, 3–15.

362 Lorenz, R., Bock, J., A. J. Barker, e.a., 2014. 4d flow magnetic resonance imaging in bicuspid aortic  
363 valve disease demonstrates altered distribution of aortic blood flow helicity. *Magn. Reson. Med.*  
364 71, 1542 – 53.

365 Manuel, J., Tavares, R.S., Jorge, R.M.N., 2009. *Computational Vision and Medical Image Processing.*  
366 CRC Press ISBN 9780415570411.

367 Meierhofer, C., Schneider, E.P., Lyko, C., Hutter, A., Martinoff, S., Markl, M., Hager, A., Hess, J.,  
368 Stern, H., Fratz, S., 2012. Wall shear stress and flow patterns in the ascending aorta in patients  
369 with bicuspid aortic valves differ significantly from tricuspid aortic valves: a prospective study.  
370 *European Heart Journal - Cardiovascular Imaging* 14(8), 797–804.

371 Morbiducci, U., Ponzini, R., Gallo, D., Bignardi, C., Rizzo, G., 2013. Inflow boundary conditions for

372 image-based computational hemodynamics: Impact of idealized versus measured velocity profiles  
373 in the human aorta. *J. Biomech.* 46, 102–109.

374 Morbiducci, U., Ponzini, R., Grigioni, M., Redaelli, A., 2007. Helical flow as fluid dynamic signature  
375 for atherogenesis in aorto coronary bypass.a numeric study. *J. Biomech.* 40, 519–534.

376 Muraru, D., Bidviene, J., Cavalli, G., Cavaliere, A., Badano, L.P., 2016. Tricuspid regurgitation in a  
377 patient with ascending aorta aneurysm. *Euro. Heart J. Cardiovasc. Imag.* 17, 1435.

378 Nordgaard, H., Swillens, A., Nordhaug, D., Garstad, I.K., Loo, D.V., Vitale, N., Segers, P., Haaverstad,  
379 R., 2010. Impact of competitive flow on wall shear stress in coronary surgery: computational fluid  
380 dynamics of a LIMA-LAD model. *Cardiovascular Research* 88, 512–519.

381 Numata, S., Itatani, K., Kanda, K., Doi, K., Yamazaki, S., Morimoto, K., Manabe, K., Ikemoto, K.,  
382 Yaku, H., 2016. Blood flow analysis of the aortic arch using computational fluid dynamics. *Euro.*  
383 *J. Cardio. Thora.surg* 49, 1578–1585.

384 Ooij, P.V., Markl, M., Collins, J.D., Carr, J.C., Rigsby, C., Bonow, R.O., Malaisrie, S.C., McCarthy,  
385 P.M., Fedak, P.W.M., Barker, A.J., 2017. Aortic valve stenosis alters expression of regional aortic  
386 wall shear stress: New insights from a 4-dimensional flow magnetic resonance imaging study of  
387 571 subjects. *J. Amer. Heart Assoc.* 6, e005959.

388 Papadopoulos, K.P., Gavaises, M., Pantos, I., Katritsis, D.G., Mitroglou, N., 2016. Derivation of flow  
389 related risk indices for stenosed left anterior descending coronary arteries with the use of computer  
390 simulations. *Med. Eng. Phy* 38, 929–939.

391 Pasta, S., Phillippi, J.A., Gleason, T.G., Vorp, D.A., 2012. Effect of aneurysm on the mechanical  
392 dissection properties of the human ascending thoracic aorta. *J. Thorac. Cardiovasc. Surg.* 143,  
393 460–467.

394 Pasta, S., Rinaudo, A., Luca, A., Pilato, M., Scardulla, C., Gleason, T.G., Vorp, D.A., 2013. Difference

395 in hemodynamic and wall stress of ascending thoracic aortic aneurysms with bicuspid and tricuspid  
396 aortic valve. *J. Biomech.* 46, 1729 – 1738.

397 Pedersen, M.W., Groth, K.A., Mortensen, K.H., Broderson, J., Gravholt, C.H., Andersen, N.H., 2019.  
398 Clinical and pathophysiological aspects of bicuspid aortic valve disease. *Cardiology Young* 29, 1  
399 – 10.

400 Pirola, S., Jarral, O.A., Regan, D.P.O., Asimakopulos, G., Anderson, J.R., Pepper, J.R., Athanasiou,  
401 T., Xu, X.Y., 2018. Computational study of aortic hemodynamics for patients with an abnormal aor-  
402 tic valve: The importance of secondary flow at the ascending aorta inlet. *APL Bioeng.* 2, 026101–1  
403 – 026101–14.

404 Real, E., Val-Bernal, J.F., Revuelta, J.M., Ponton, A., Diez, M.C., Mayorga, M., Higuera, J.M.L.,  
405 Conde, O.M., 2014. Identification of vessel wall degradation in ascending thoracic aortic  
406 aneurysms with OCT. *Biomed. Opt. Ex.* 5, 1 – 12.

407 Romarowski, R.M., Lefieux, A., Morganti, S., Veneziani, A., Auricchio, F., 2018. Patient-  
408 specific CFD modelling in the thoracic aorta with pc-mri-based boundary conditions: A  
409 least-square three-element windkessel approach. *Int. J. Numer. Methods. Biomed. Eng.*  
410 <https://doi.org/10.1002/cnm.3134>.

411 Sigovan, M., Hope, M.D., Dyverfeldt, P., Saloner, D., 2011. Comparison of Four-Dimensional Flow  
412 Parameters for Quantification of Flow Eccentricity in the Ascending Aorta. *J. Mag. Res. Imag.* 34,  
413 1226–1230.

414 Simao, M., Ferreira, J.M., Tomas, A.C., Fragata, J., Ramos, H.M., 2017. Aorta Ascending Aneurysm  
415 Analysis Using CFD Models towards Possible Anomalies. *Fluids* 2, 1–15.

416 Stankovic, Z., Allen, B.D., Garcia, J., Jarvis, K.B., Markl, M., 2014. 4D flow imaging with MRI.  
417 *Cardio. Diagn. Therap.* 4, 173–192.

418 Steinman, D.A., 2012. Assumptions in modelling of large artery hemodynamics. Springer, Milano.

419 Stevens, R.R.F., Grytsan, A., Biasseti, J., Roy, J., Liljeqvist, M.L., Gasser, T.C., 2017.

420 Biomechanical changes during abdominal aortic aneurysm growth. PLoS ONE

421 <https://doi.org/10.1371/journal.pone.0187421>.

422 Stonebridge, P.A., Hoskins, P.R., Allan, P.L., Belch, J.F., 1996. Spiral laminar flow in vivo. Clinical

423 Science 91, 17–21.

424 Tarbell, J.M., 2003. Mass transport in arteries and the localization of atherosclerosis. Annu. Rev.

425 Biomed. Eng. 5, 79–118.

426 Torii, R., Keegan, J., Wood, N.B., Dowsey, A.W., Hughes, A.D., Yang, G.Z., Firmin, D.N., Thom,

427 A.M., Xu, X.Y., 2009. The effect of dynamic vessel motion on haemodynamic parameters in the

428 right coronary artery: a combined MR and CFD study. British Journal of Radiology 82, S24–S32.

429 Weigang, E., Kari, F.A., Beyersdorf, F., Luehr, M., Etz, C.D., Frydrychowicz, A., Harloff, A., Markl,

430 M., 2008. Flow-sensitive four-dimensional magnetic resonance imaging: flow patterns in ascending

431 aortic aneurysms. Euro. J. Cardio. Thora.surg 34, 11–16.

432 Youssefi, P., Gomez, A., Arthurs, C., Sharma, R., Jahangiri, M., Figueroa, C.A., 2018. Impact of

433 patient-specific inflow velocity profile on hemodynamics of the thoracic aorta. J. Biomech. Eng.

434 140, 011002–1 – 011002–14.

435 Youssefi, P., Gomez, A., He, T., Anderson, L., Bunce, N., Sharma, R., Figueroa, C.A., Jahangiri,

436 M., 2017. Patient-specific computational fluid dynamics-assessment of aortic hemodynamics in a

437 spectrum of aortic valve pathologies. J. Thorac. Cardiovasc. Surg. 153, 8–20e23.

438 Yu, S.C., Liu, W., Wong, R.H., Underwood, M., Wang, D., 2016. The Potential of Computational

439 Fluid Dynamics Simulation on Serial Monitoring of Hemodynamic Change in Type B Aortic Dis-

440 section. Cardiovasc. Intervent. Radiol. 39, 1090–1098.

## FIGURE CAPTIONS

- 441
- 442 Fig.1 Time-averaged velocity profiles obtained from 4D flow MRI and CFD at the inlet. The dorsal  
443 (D), ventral (V), anterior (A) and posterior (P) regions are defined according to Fig. S1 in the  
444 supplementary materials.
- 445 Fig.2 Bland-Altman plot showing 4D flow MRI vs CFD  $Flow_{eccentricity}$  obtained from time-averaged  
446 velocity profiles near the ATA region.
- 447 Fig.3 Streamlines of blood velocity at peak systole for TAV ATAA, BAV ATAA and healthy subjects.
- 448 Fig.4 TAWSS and LNH distribution in the ATA region for TAV ATAA patients.
- 449 Fig.5 TAWSS and LNH distribution in the ATA region for BAV ATAA patients.
- 450 Fig.6 TAWSS and LNH distribution in the ATA region for healthy subjects.
- 451 Fig.7 Correlation between the flow eccentricity near the dilated region and other significant parameters  
452 (hemodynamics and morphology).
- 453 Fig.8 Correlation between the maximum ATAA diameter and hemodynamics parameters.

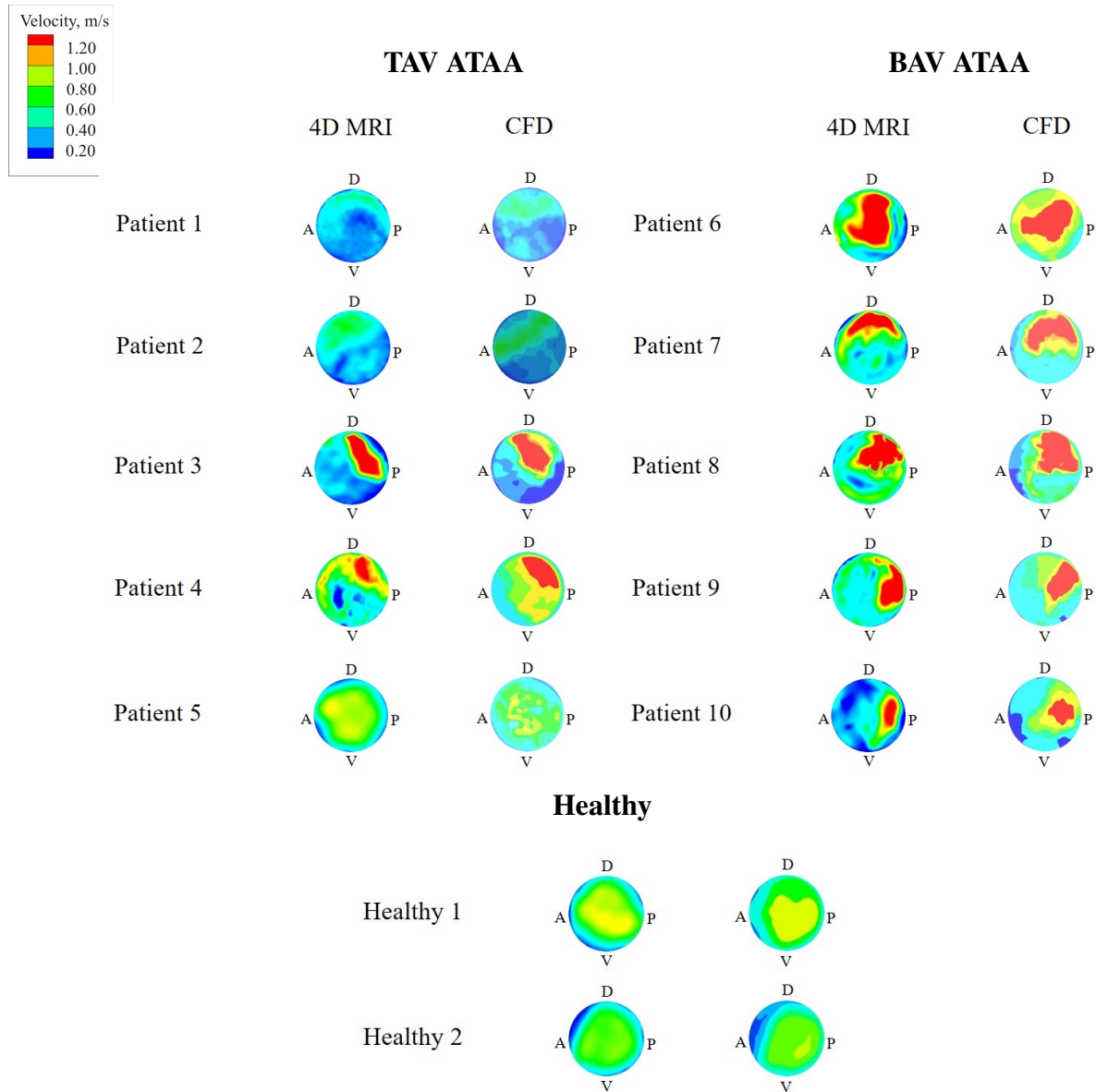


Fig. 1. Time-averaged velocity profiles obtained from 4D flow MRI and CFD at the inlet. The dorsal (D), ventral (V), anterior (A) and posterior (P) regions are defined according to Fig. S1 in the supplementary materials

454

455

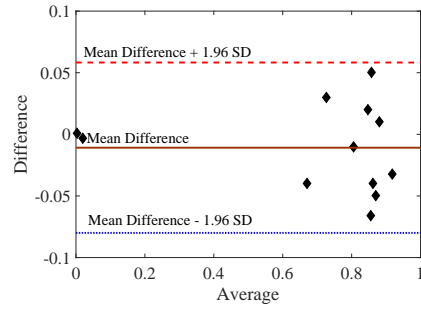


Fig. 2. Bland-Altman plot showing 4D flow MRI vs CFD  $Flow_{eccentricity}$  obtained from time-averaged velocity profiles near the ATA region.

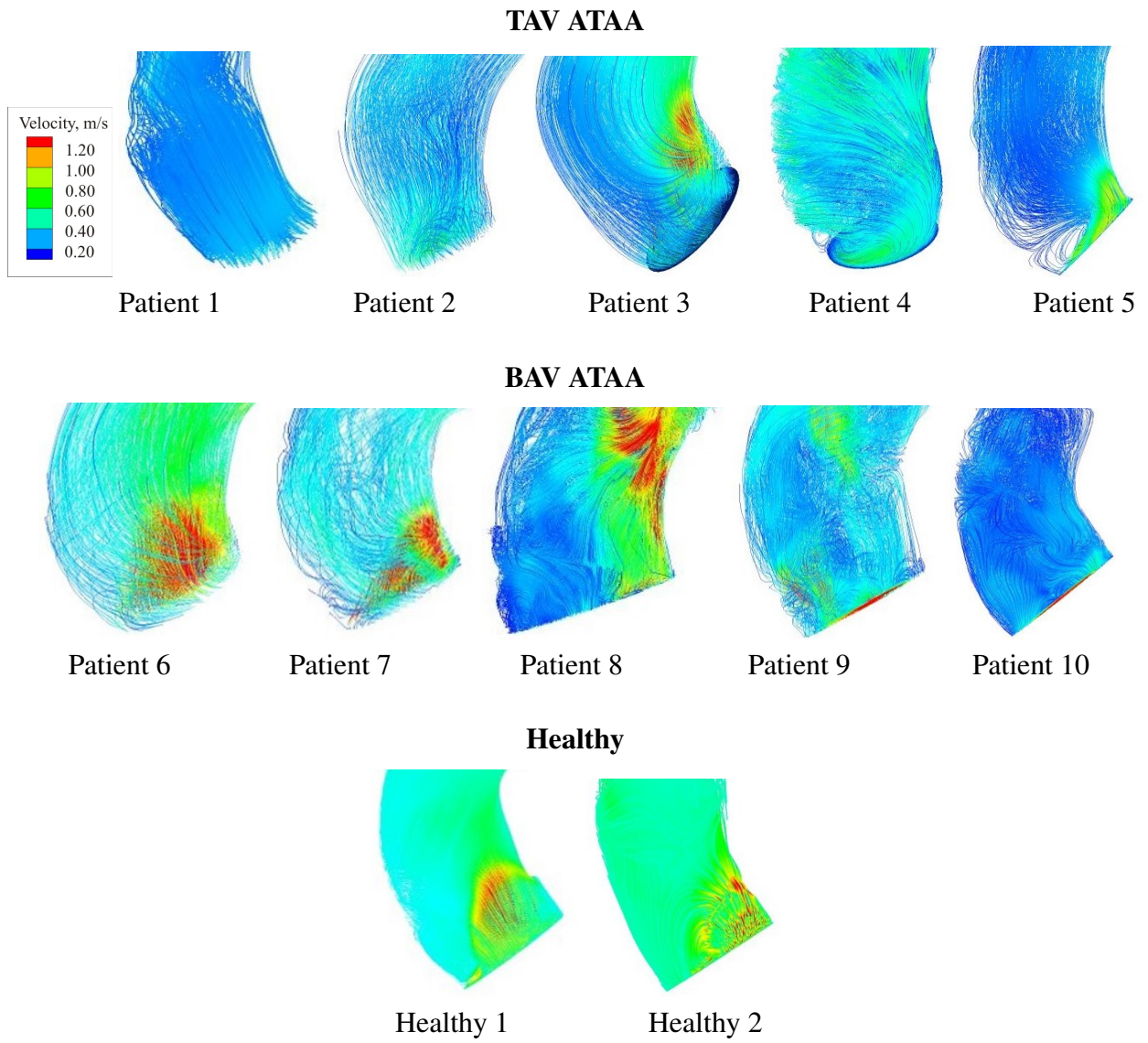


Fig. 3. Streamlines of blood velocity at peak systole for TAV ATAA, BAV ATAA and healthy subjects.

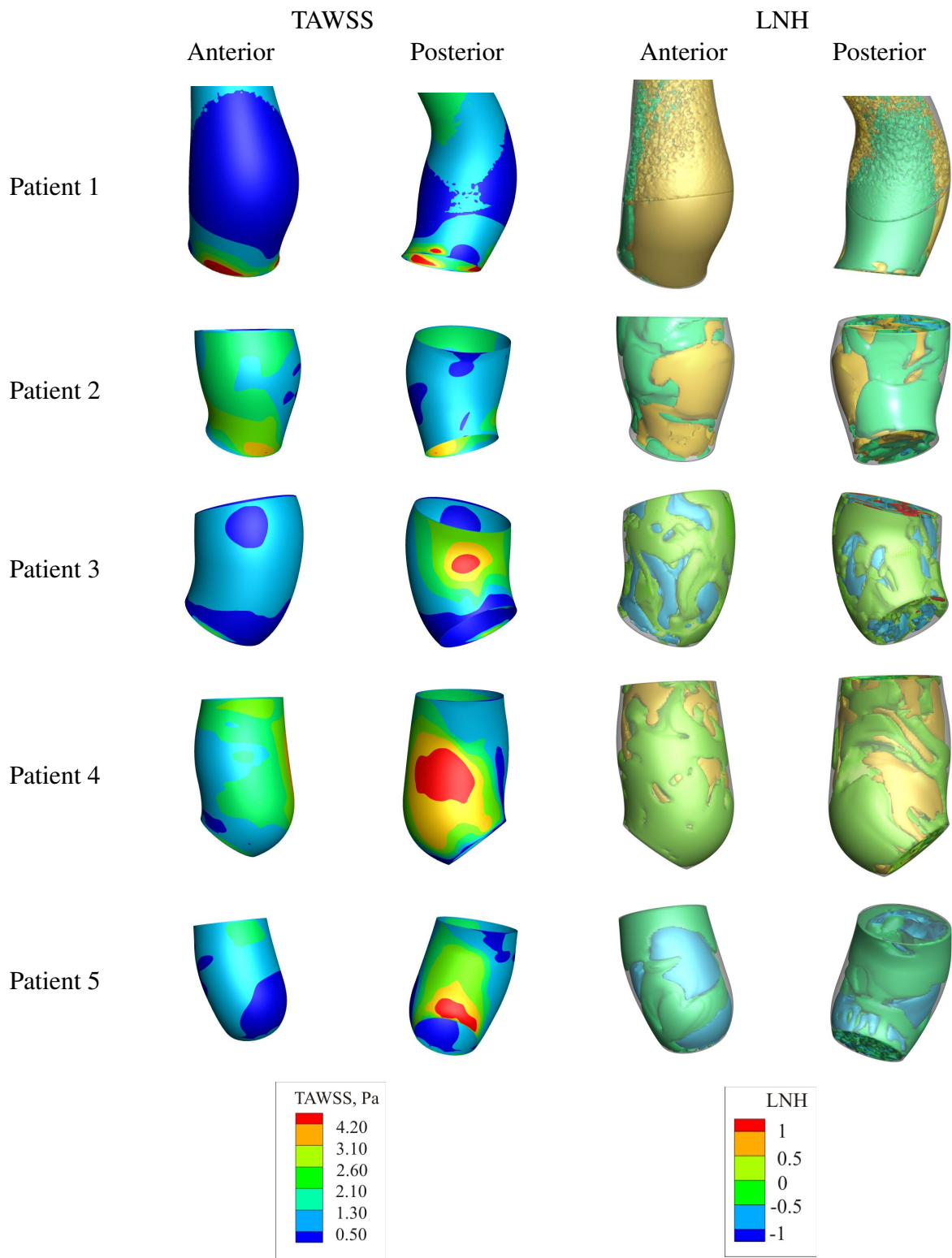


Fig. 4. TAWSS and LNH distribution in the ATA region for TAV ATAA patients.

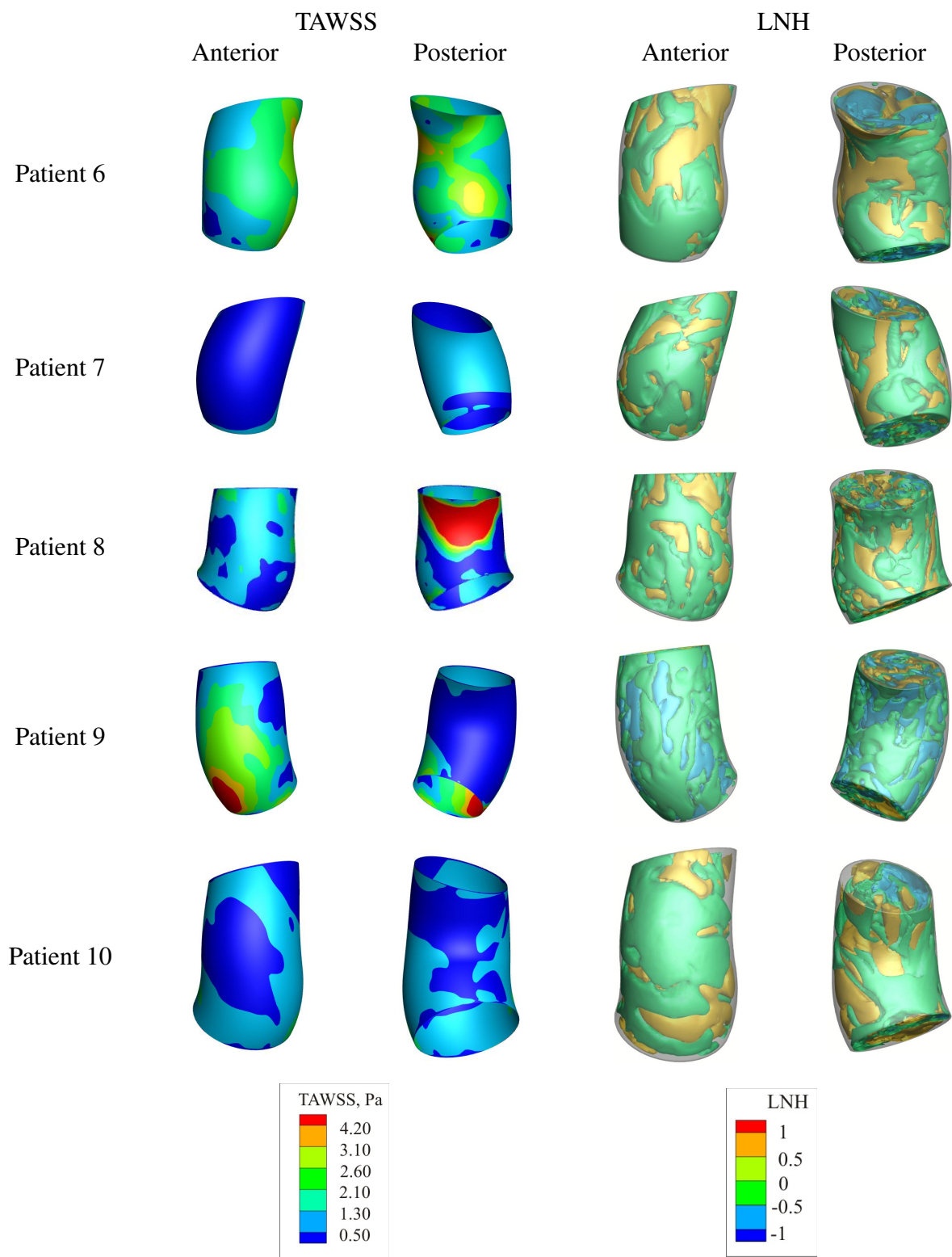


Fig. 5. TAWSS and LNH distribution in the ATA region for BAV ATAA patients.

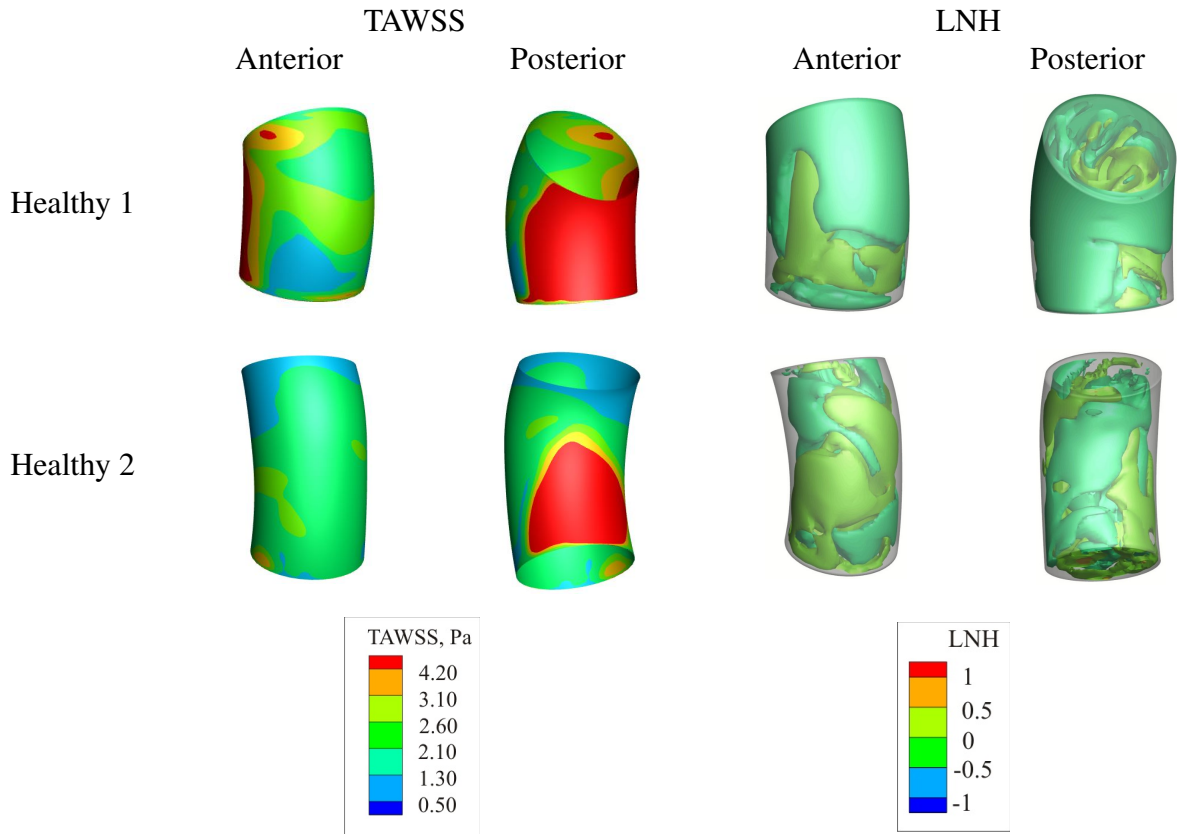


Fig. 6. TAWSS and LNH distribution in the ATA region for healthy subjects.

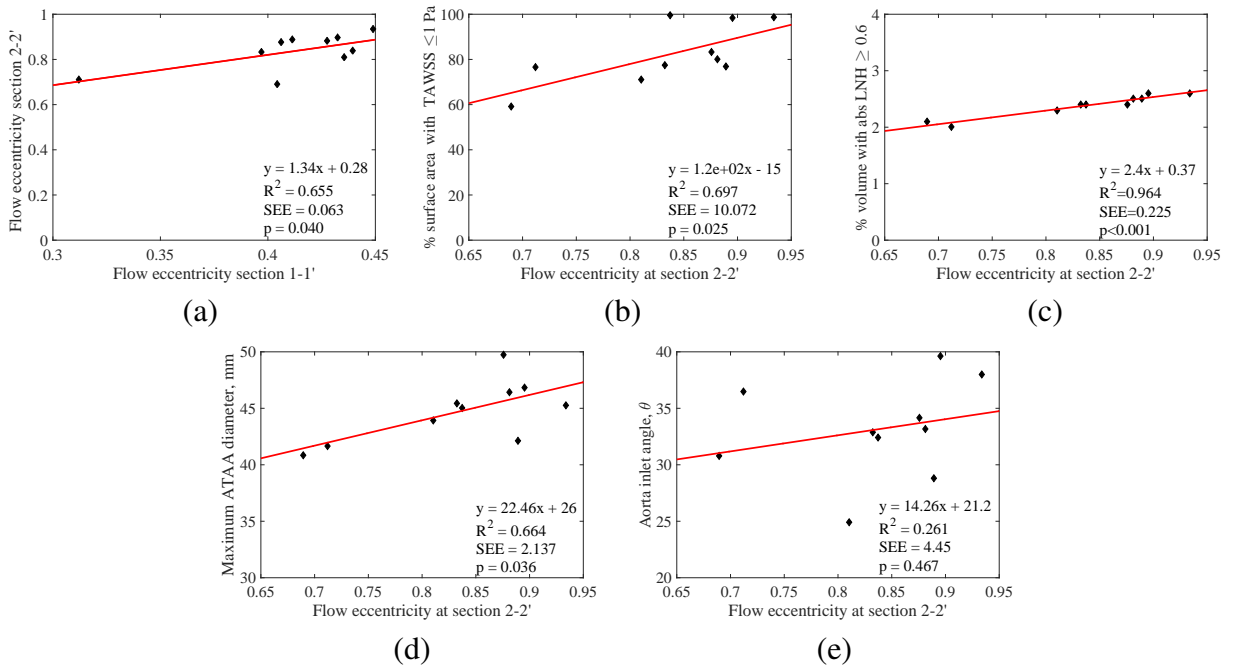


Fig. 7. Correlation between the flow eccentricity near the dilated region and other significant parameters (hemodynamics and morphology)

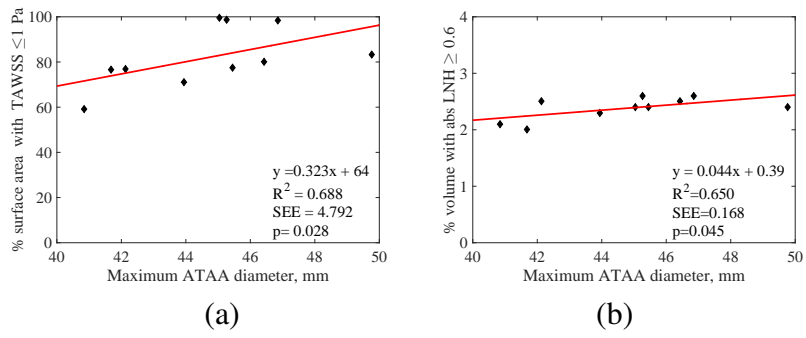


Fig. 8. Correlation between the maximum ATAA diameter and hemodynamic parameters

459

## TABLE CAPTIONS

460 Tab.1 Test of significance for TAV ATAA versus BAV ATAA patient characteristics and hemodynamics  
461 descriptors.

462 Tab.2 Percentage of TAWSS area and absolute LNH volume for TAV ATAA, BAV ATAA patients and  
463 healthy subjects.

Table 1

Test of significance for TAV ATAA versus BAV ATAA patient characteristics and hemodynamics descriptors.

	Parameters	TAV ATAA	BAV ATAA	Sig (2-tailed) TAV ATAA vs BAV ATAA
Patient characteristics	Age, Years	59.60 ± 11.63	58.20 ± 5.59	0.817
	Weight, Kg	75.40 ± 18.63	73.20 ± 11.38	0.829
	Height, m	1.67 ± 0.13	1.66 ± 0.03	0.779
	BSA	1.85 ± 0.26	1.83 ± 0.14	0.855
	Maximum ATAA diameter, mm	43.94 ± 3.66	45.55 ± 1.14	0.393
	Inlet angle, $\theta$	33.65 ± 3.84	32.59 ± 5.21	0.725
Hemodynamics parameters	Flow eccentricity at section 1-1'	0.39 ± 0.05	0.43 ± 0.01	0.268
	Flow eccentricity at section 2-2'	0.82 ± 0.11	0.85 ± 0.03	0.575
	% Surface area with TAWSS $\geq$ 3 Pa	0.33 ± 0.49	3.08 ± 4.05	0.282
	% Surface area with TAWSS $\leq$ 1 Pa	78.96 ± 14.19	85.28 ± 12.95	0.483
	% Volume with absolute LNH $\geq$ 0.6	2.02 ± 1.96	1.11 ± 0.53	0.367
	% Volume with absolute LNH $\leq$ 0.4	88.50 ± 6.72	93.38 ± 5.21	0.235

Table 2

Percentage of TAWSS area and absolute LNH volume for TAV ATAA, BAV ATAA patients and healthy subjects.

		% surface area with TAWSS		% volume with absolute LNH	
		$\geq 3$ Pa	$\leq 1$ Pa	$\geq 0.6$	$\leq 0.4$
TAV ATAA	Patient 1	0.10	98.7	2.10	90.4
	Patient 2	0.12	76.8	2.60	89.4
	Patient 3	0.10	83.4	2.10	91.5
	Patient 4	1.20	59.3	3.10	80.9
	Patient 5	0.15	76.6	5.50	82.3
BAV ATAA	Patient 6	8.00	71.0	3.10	85.0
	Patient 7	0.15	99.7	2.40	91.9
	Patient 8	7.00	80.0	2.10	93.8
	Patient 9	0.15	77.4	2.80	94.2
	Patient 10	0.10	98.3	2.10	93.2
Healthy	Healthy 1	28.5	20.5	0.50	98.6
	Healthy 2	27.3	20.1	0.40	98.7

## 464 7 Supplementary Materials

### 465 A Materials and Methodology

#### 466 A.1 4D flow MRI Data acquisition

467 4D flow MRI datasets consists of magnitude data representing the patients aortic anatomy and phase  
468 data representing the velocities along  $V_x$ ,  $V_y$  &  $V_z$  (Fig. S3) obtained throughout the cardiac cycle  
469 thus providing a dynamic imaging of the blood flow. 4D flow MRI data acquisition requires efficient  
470 scan times which synchronizes between cardiac and respiratory movements (Stankovic et al., 2014)  
471 in order to obtain good images. The ECG gating and the imaging parameters for 4D flow MRI data  
472 acquisition are as follows: spatial resolution =  $2.4 \times 2.4 \times 2.4 \text{ mm}^3$ , field of view (FOV) =  $380 \times$   
473  $285 \text{ mm}^2$ , velocity encoding (VENC) = 200 cm/s, Bandwidth (BW) = 496 Hz/Pixel, Flip angle =  $7^\circ$ ,  
474 echo time (TE) / repetition time (TR) = 2.19 / 37.9 and phase duration (Temporal resolution) = 37.9  
475 ms.

#### 476 A.2 Pre-procssing of 4D flow MRI data

477 The data obtained from 4D flow MRI may have some artifacts that can degrade the image quality and  
478 flow measurements hence appropriate correction strategies are to be employed in order to be used in  
479 the simulation (Stankovic et al., 2014). 4D flow MRI datasets were analyzed using the Velocity Map-  
480 ping Tool (Tool for preprocessing & converting of 4D Flow MRI data- Freiburg University, Germany  
481 & Northwestern University, USA) in combination with MATLAB (MathWorks Inc. R2015b). This

482 tool helps us to apply the eddy-current correction, noise filter to improve the quality of the image and  
483 the pre-processed data were imported into 3D visualization software (Enlight, CEI, Inc.), to obtain  
484 dynamic visualization and extraction of velocity profiles (Fig. S3).

### 485 *A.3 3D Velocity profile extraction*

486 Enlight is a commercial tool used to extract the 3D velocity profiles from the 4D flow MRI mea-  
487 sured data. 2D analysis cross-sectional plane were introduced (i.e ascending aorta and apico-aortic  
488 branches such as brachiocephalic artery (BCA), left common carotid artery (LCC) & left subclavian  
489 artery (LSUB)) on the pre-processed image obtained from velocity mapping tool (Fig. S3). On these  
490 planes, the 3D blood flow velocity vector field were projected for each individual cardiac time-frame.  
491 The magnitude and velocity vectors obtained from these planes were post processed using Matlab.  
492 The obtained patient-specific velocity maps and flow rate waveforms were given as input boundary  
493 conditions to the CFD simulation.

### 494 *A.4 Aorta reconstruction and meshing*

495 The 3D aorta model was reconstructed from the 4D flow MRI data using a semi-automatic segmenta-  
496 tion in the CRIMSON (Cardiovascular Integrated Modelling and SimulatiON) tool where a center-  
497 line was positioned along the entire length of the aorta starting from the aortic root to the descending  
498 aorta. The analysis planes were automatically distributed along the center-line after manually select-  
499 ing the points along the center-line and they were oriented normal to the aorta. These analysis planes  
500 were useful for tracking the cross section of the aorta at the respective points. The reconstructed

501 patient-specific geometry, including the ascending thoracic aorta, aortic arch with branches and the  
502 descending aorta, was imported in Ansys-Fluent (ANSYS, Academic research, Release 17.2) and  
503 meshed with 1.5-6.2 millions of tetrahedral elements (Fig. S3). A convergence analysis was carried  
504 out to obtain mesh independent analyses.

#### 505 *A.5 CFD analysis and simulation setup*

506 The finite volume method (FVM) was used to solve the governing equations of the fluid motion under  
507 unsteady flow conditions in Ansys Fluent. The blood flow was assumed to be laminar, non-Newtonian  
508 and incompressible with a density of  $1050 \text{ kg/m}^3$ . The details regarding the model and the parameters  
509 used in this simulation can be obtained from Jayendiran et al. (2020).

510 Patient-specific 4D flow MRI data were used to define the inflow velocity profile. Pixel-based time-  
511 varying velocities were obtained from these phase-contrast flow maps. The 3D velocity profiles ( $V_x$ ,  
512  $V_y$  &  $V_z$ ) were extracted from these phase-contrast flow maps by using an in-house Matlab code  
513 (MathWorks Inc. R2015b) and mapped onto the inlet face of the aorta (Fig. S4). Therefore, every  
514 voxel of the aorta inlet section was assigned a velocity vector whose direction and magnitude was  
515 determined from the PC-MRI data. The patient-specific flow rate obtained from 4D flow MRI was  
516 assigned at the outlet sections of the apico-aortic branches (BCA, LCC, LSUB) (Morbiducci et al.,  
517 2013; Youssefi et al., 2017) as outflow boundary conditions (Fig. S4). A multiscale approach was  
518 implemented to describe the hemodynamics at the descending aorta outlet by coupling the 3D domain  
519 with a reduced order model (i.e three element Windkessel model). The three-element Windkessel  
520 model was assigned to represent the targeted physiological blood pressure measured from the patients  
521 during the 4D flow MRI data acquisition (Fig. S4). Given a target diastolic and systolic pressure

522 (measured from the patients during the 4D flow MRI data acquisition), the value of the impedance  
523 (Z), the distal resistance (R) and the capacitor (C) were adjusted in an iterative manner so that the  
524 predicted flow distributions in each vascular region were within 3% of 4D flow MRI measurements.  
525 The outlet boundary meshes were extended 20 times the length of their diameter for sufficient pressure  
526 recovery. The aortic walls were assumed to be rigid, impermeable and with no-slip.

527 The solution of Navier-Stokes equations was obtained with Ansys Fluent v17.2 using the Semi-  
528 Implicit Method for Pressure-Linked Equations (SIMPLE), a second-order interpolation scheme and  
529 a second-order upwind interpolation. A second order implicit time advanced scheme was used as  
530 transient-time solver and a time step size  $\Delta t$  of 1 ms was chosen. This time step size is fine enough to  
531 capture the time-dependent flow parameters accurately and to ensure that the convergence is reached  
532 with the assigned maximum number of iterations per time step. The appropriate time step size was  
533 evaluated as follows (Ansys Fluent):

$$\Delta t \approx \frac{\textit{Typical cell size}}{\textit{Characteristic flow velocity}} \quad (\text{A.1})$$

534 The convergence of the solution was assessed for relative residual errors below  $10^{-3}$ . A residual  
535 plot for the transient flow simulation is shown in Fig. S5. The initial guess and the time step size  
536 were chosen in such a way that the residuals reduce by around three orders of magnitude within one  
537 time step and stabilizes after the few iterations providing accurate resolution of transient behavior. To  
538 ensure fully developed flow and to avoid unsteady state solution due to initial transient conditions, the  
539 simulation was performed for three cardiac cycles and the last cycle was used for post-processing.

## 540 **B Patient characteristics**

541 The patient-specific aortic geometry was reconstructed using 4D flow MRI and the maximum ATA di-  
542 ameter was measured for each subject. In order to optimize measurement accuracy, the ATA diameter  
543 was measured several times from 4D MRI data sets and uncertainty in the measurements was esti-  
544 mated. We performed 10 multiple measurements for each subject. Details regarding the uncertainty  
545 analysis and the estimation of maximum ATA diameter can be found in Jayendiran et al. (2020).

546 The inlet angle  $\theta$  was measured using a horizontal plane placed at the aortic root and the inclination  
547 made by the aortic inlet with respect to the horizontal plane gave us the  $\theta$  (Fig. S4). The measurement  
548 of this angle was introduced in Condemi et al. (2019).

549 The comparison of patient characteristics in TAV and BAV groups are reported in Tab. 1. The param-  
550 eters such as age ( $p = 0.817$ ), weight ( $p = 0.829$ ), height ( $p = 0.779$ ), Body Surface Area (BSA) ( $p =$   
551  $0.855$ ), maximum ATAA diameter ( $p = 0.393$ ) and inlet angle ( $p = 0.725$ ) all have a  $p$ -value  $> 0.05$ . In  
552 this study the significance ( $p > 0.05$ ) value shows that the TAV and BAV patient characteristics were  
553 not significantly different. In the TAV group, two patients presented mild degree of aortic regurgita-  
554 tion (AR) and only one a mild degree of aortic stenosis (AS) (mean gradient = 10 mmHg). In the BAV  
555 group only two patients presented a mild degree of AR (Tab. S1 in the supplementary materials).